

Omni-LIVO: Robust RGB-Colored Multi-Camera Visual-Inertial-LiDAR Odometry via Photometric Migration and ESIKF Fusion

Yinong Cao¹, Xin He^{1,*}, Yuwei Chen^{2,*}, Chenyang Zhang¹, Chengyu Pu¹, Bingtao Wang¹,
Kaile Wu¹, Shouzheng Zhu¹, Fei Han², Shijie Liu¹, Chunlai Li¹ and Jianyu Wang^{1,3}

Abstract—Wide field-of-view (FoV) LiDAR sensors provide dense geometry across large environments, but most existing LiDAR-inertial-visual odometry (LIVO) systems rely on a single camera, leading to limited spatial coverage and degraded robustness. We present Omni-LIVO, the first tightly coupled multi-camera LIVO system that bridges the FoV mismatch between wide-angle LiDAR and conventional cameras. Omni-LIVO introduces a Cross-View direct tracking strategy that maintains photometric consistency across non-overlapping views, and extends the Error-State Iterated Kalman Filter (ESIKF) with multi-view updates and adaptive covariance weighting. The system is evaluated on public benchmarks and our custom dataset, showing improved accuracy and robustness over state-of-the-art LIVO, LIO, and visual-inertial baselines. Code and dataset will be released upon publication.

Index Terms—SLAM, multi-camera system, tightly coupled, visual-inertial-LiDAR fusion, direct visual methods, voxel map.

I. INTRODUCTION

SIMULTANEOUS Localization and Mapping (SLAM) has become essential for autonomous systems operating in unknown environments. Traditional methods are categorized by sensor types: vision-based SLAM [1], [2] provides rich photometric information but struggles in low-light or texture-poor scenes, while LiDAR-based SLAM [3]–[5] offers robust geometry but degrades in repetitive environments. IMUs, though environment-independent, suffer from long-term drift.

To address single-sensor limitations, multi-sensor fusion systems like visual-inertial SLAM (VI-SLAM) and LiDAR-inertial SLAM (LI-SLAM) enhance robustness through complementary sensor properties [6], [7]. Recent LIVO systems combine dense LiDAR geometry, camera photometrics, and high-frequency IMU measurements [8], [9].

However, a fundamental mismatch persists: wide-FoV LiDAR sensors (360°) are paired with narrow-FoV cameras (60-120°), creating spatial coverage gaps that limit tracking robustness during aggressive maneuvers or in occluded environments.

This FoV mismatch causes critical limitations. When photometric patches exit the narrow camera FoV, direct visual constraints are lost, forcing reliance solely on LiDAR geometry—problematic in texture-rich but geometrically repetitive environments. Single-camera systems also lose patch continuity during rapid rotations when wide-FoV LiDAR data could provide maximum benefit.

While multi-camera systems have been explored in visual SLAM [10], [11], their tight integration with LiDAR and inertial data in LIVO systems remains underexplored. The key challenge is maintaining photometric continuity across non-overlapping views, requiring temporal feature migration as features disappear from one camera and reappear in another. Additionally, standard ESIKF formulations assume uniform measurement quality, while multi-camera integration demands adaptive covariance modeling for heterogeneous measurement reliability.

To address these challenges, we present Omni-LIVO, the first tightly coupled multi-camera LIVO system built on FAST-LIVO2 [12] that bridges the FoV mismatch between wide-angle LiDAR and narrow camera views.

The main contributions are:

- 1) **Cross-View temporal migration**: A direct tracking strategy preserving photometric consistency across non-overlapping views.
- 2) **Adaptive multi-view ESIKF**: Enhanced ESIKF with adaptive covariance weighting for improved robustness in adverse conditions.
- 3) **Unified voxel representation**: Integration of LiDAR geometric and multi-view visual constraints within a single volumetric structure.
- 4) **Comprehensive evaluation**: Omni-LIVO completes all 14 sequences from Hilti SLAM Challenge [24] and Newer College datasets [25], achieving lowest RMSE on 12 sequences with average 34% accuracy improvement over FAST-LIVO2.

II. RELATED WORKS

A. LiDAR-Inertial Odometry Evolution

LiDAR-inertial odometry (LIO) systems have evolved from loosely coupled to tightly integrated frameworks. Early works like LOAM [3] introduced real-time LiDAR odometry via feature extraction and scan-to-scan matching. LeGO-LOAM

*Corresponding author: Xin He (e-mail: xinhe@ucas.ac.cn); Yuwei Chen (e-mail: yuwei.chen@ucas.ac.cn)

¹Hangzhou Institute for Advanced Study, University of Chinese Academy of Sciences, Hangzhou 310024, China.

²Advanced Laser Technology Lab of Anhui Province, Hefei 230026, China.

³Key Laboratory of Space Active Opto-Electronics Technology, Shanghai Institute of Technical Physics, Chinese Academy of Sciences, Shanghai 200083, China

[13] enhanced this by incorporating IMU data for motion compensation and loop closure detection. The paradigm has shifted toward direct methods with FAST-LIO [14], which eliminated feature extraction and directly registered raw points to maps using an iterated Kalman filter. FAST-LIO2 [15] further improved computational efficiency and robustness through incremental map updates and adaptive voxelization.

While these LIO systems achieve excellent geometric accuracy, they lack the rich photometric information necessary for robust operation in geometrically degraded environments such as long corridors, open areas, or scenes with repetitive structures.

B. LiDAR-Visual-Inertial Integration

To address the limitations of pure LIO systems, researchers have explored LiDAR-visual-inertial fusion. RÅ²LIVE [16] introduced direct image alignment into an iterated Kalman filter framework, while R3LIVE [17] extended this with RGB-color consistency. FAST-LIVO [9] pioneered the tight coupling of LiDAR and visual data by attaching image patches to LiDAR map points and minimizing direct photometric errors. FAST-LIVO2 [12] refined this approach through a sequential update strategy in the ESIKF, employing direct methods for both LiDAR and visual modules without feature extraction.

However, all existing LIVO systems are inherently designed for single-camera configurations, creating a fundamental architectural limitation when paired with wide FoV LiDAR sensors.

C. Multi-Camera Visual-Inertial Systems

Recognizing the spatial coverage limitations of monocular systems, multi-camera visual-inertial SLAM has gained significant attention. MIMC-VINS [18] supports arbitrary numbers of uncalibrated cameras using multi-state constraint Kalman filtering. BAMF-SLAM [19] tightly integrates multiple fisheye cameras with IMU through bundle adjustment optimization. MAVIS [11] introduces SE₂(3)-based IMU pre-integration with inter-camera loop constraints for real-time performance.

While these systems expand spatial perception and improve tracking robustness, they operate purely in the visual-inertial domain and cannot leverage the dense geometric structure provided by LiDAR sensors, limiting their accuracy in texture-poor environments.

D. Direct Visual Methods

Direct visual methods estimate motion by minimizing photometric error over image intensities without explicit feature extraction. Seminal works include DTAM [20] for dense tracking and LSD-SLAM [1] for semi-dense estimation. DSO [21] and its stereo variant [22] improved robustness through sparse point selection and photometric calibration. MultiCol-SLAM [23] extended direct methods to multi-camera systems with arbitrary configurations.

The direct approach is particularly suitable for multi-camera LIVO systems as it avoids the complexity of feature correspondence across non-overlapping views while enabling dense photometric constraints that complement LiDAR's geometric structure.

III. SYSTEM OVERVIEW AND METHODOLOGY

Our approach bridges the field-of-view mismatch between wide-angle LiDAR sensors and narrow-FoV cameras through Cross-View temporal migration and multi-view ESIKF integration. We leverage direct visual tracking methods extended to multi-camera configurations to maintain photometric continuity across non-overlapping views. We present our multi-sensor synchronization strategy, Cross-View temporal migration, LiDAR geometric constraints, unified voxel mapping, and adaptive multi-view ESIKF formulation.

The overall system pipeline is illustrated in Fig. 1.

A. Multi-Sensor Data Synchronization

To achieve consistent fusion across LiDAR, cameras, and IMU, we adopt a unified synchronization strategy. The system forms temporally coherent measurement packets:

$$\mathcal{M}_k = \{\mathcal{P}_k^{\text{seg}}, \{\mathcal{J}_j\}_{j=k-1}^k, \{\mathcal{C}_k^{(i)}\}_{i=1}^4\} \quad (1)$$

where $\mathcal{P}_k^{\text{seg}}$ denotes the LiDAR point cloud temporally segmented with respect to camera exposure times, $\{\mathcal{J}_j\}_{j=k-1}^k$ represents high-frequency IMU measurements spanning the inter-frame interval, and $\{\mathcal{C}_k^{(i)}\}_{i=1}^4$ are four simultaneously triggered camera frames.

Although LiDAR and cameras may operate at the same nominal rate (e.g., 10 Hz), their trigger events are not always aligned. To align data across modalities, each LiDAR point p_i with timestamp τ_i is assigned to the temporally nearest camera frame:

$$p_i \rightarrow \mathcal{C}_j \text{ if } |\tau_i - t_{\text{cam}}^{(j)}| = \min_k |\tau_i - t_{\text{cam}}^{(k)}| \quad (2)$$

All camera channels are externally triggered to ensure simultaneous exposure:

$$t_{\text{cam}}^{(1)} = t_{\text{cam}}^{(2)} = t_{\text{cam}}^{(3)} = t_{\text{cam}}^{(4)} = t_{\text{sync}} \quad (3)$$

Eqs. (1)-(3) define the segmentation and alignment process, ensuring that LiDAR points, camera frames, and IMU priors are temporally consistent within a unified packet, as illustrated in Fig. 2.

B. Cross-View Direct Method

Single-camera photometric constraints are lost when patches exit the field of view. We formalize Cross-View temporal migration and photometric alignment to maintain continuity across non-overlapping views, as illustrated in Fig 3. The migration condition is given in Eq. (4), where a patch is considered migrated from camera i to j if it disappears from the former and reappears in the latter while satisfying visibility and temporal constraints:

$$M(\mathbf{p}, i \rightarrow j) = 1 \Leftrightarrow \begin{cases} \text{cam}_{\text{ref}}(\mathbf{p}) = i \\ \text{cam}_{\text{cur}}(\mathbf{p}) = j \\ i \neq j \\ \text{exclusive}_{\text{visible}}(\mathbf{p}, j) = 1 \\ \text{temporal}_{\text{migrated}}(\mathbf{p}, i \rightarrow j) = 1 \end{cases} \quad (4)$$

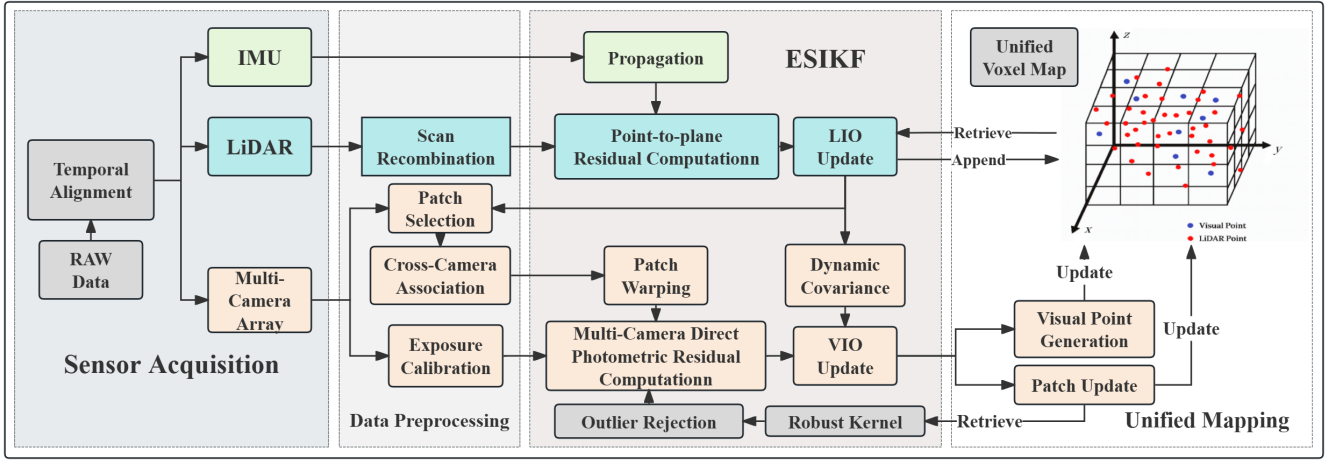


Fig. 1. Overview of the Omni-LIVO architecture. The system synchronizes multi-camera, LiDAR, and IMU data, performs scan and patch preprocessing, and employs an ESIFK framework to tightly fuse LiDAR geometric and visual photometric residuals. A unified voxel map maintains both LiDAR and visual points for consistent trajectory and map generation.

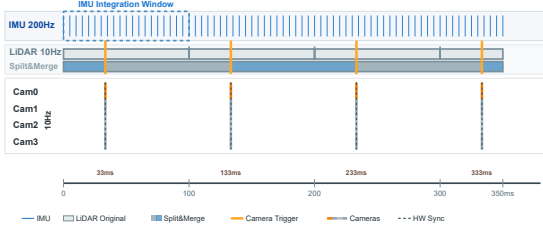


Fig. 2. Multi-sensor data synchronization in Omni-LIVO. LiDAR scans and multi-camera images, though operating at similar nominal rates, are not perfectly aligned in time. Each LiDAR point is temporally segmented and associated with the nearest camera exposure, while IMU measurements provide continuous motion priors to bridge gaps. This strategy ensures temporally consistent fusion across heterogeneous sensor streams.

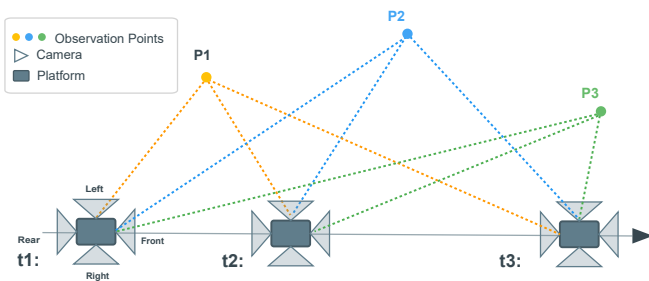


Fig. 3. Temporal migration process across multiple camera fields of view. A photometric patch initially observed in camera i disappears as it moves out of the field of view and later reappears in camera j . This migration is detected by checking temporal overlap and exclusive visibility conditions, and a Cross-View photometric residual is then established between the two observations. The illustration shows the sequential disappearance and reappearance of patches, the temporal alignment of exposures, and the association of migrated patches across different cameras.

To ensure consistent intensity comparison across cameras, image measurements are normalized by exposure and vignetting, as in Eq. (5) and Eq. (6):

$$I'_k(u, v) = \alpha_k \cdot V_k(r^2) \cdot I_k(u, v) \quad (5)$$

where α_k is the exposure scale for camera k , and $V_k(r^2)$ is a vignetting function modeled as:

$$V_k(r^2) = 1 + \sum_{n=1}^3 \beta_{k,n} \cdot r^{2n} \quad (6)$$

Mapping a point from camera i at time t_i to camera j at time t_j requires estimating the relative transformation between frames, as given by Eq. (7), and the induced homography under a local planar assumption is defined in Eq. (8):

$$\mathbf{T}_{j \rightarrow i}(t) = \mathbf{T}_j^w(t_j) \cdot (\mathbf{T}_i^w(t_i))^{-1} \quad (7)$$

$$\mathbf{H}_{i \rightarrow j}(\mathbf{p}, t) = \mathbf{R}_{j \rightarrow i}(t) + \frac{\mathbf{t}_{j \rightarrow i}(t) \mathbf{n}_i^T}{d_i} \quad (8)$$

where $\mathbf{R}_{j \rightarrow i} \in \text{SO}(3)$ is the rotation matrix, $\mathbf{t}_{j \rightarrow i} \in \mathbb{R}^3$ is the translation vector [m], $\mathbf{n}_i \in \mathbb{R}^3$ is the unit surface normal, and $d_i \in \mathbb{R}^+$ is the distance [m].

Based on these definitions, we formulate both intra-camera and Cross-View residuals, with the patch association process visualized in Fig. 4, which illustrates intra-camera consistency and Cross-View migration during turning. The direct residual within a camera is defined as:

$$r_{\text{direct}}^k(\mathbf{p}) = \gamma_{\text{cur}} \cdot I'_k(\pi_k(\mathbf{T}_k^w \cdot \mathbf{p})) - \gamma_{\text{ref}} \cdot I'_{\text{ref}}(\pi_{\text{ref}}(p_{\text{ref}})) \quad (9)$$

Cross-View temporal migration residuals establish constraints between different cameras across time:

$$r_{\text{migration}}^{i \rightarrow j}(p) = \phi_{i \rightarrow j} \cdot \tau_j \cdot I_j(\pi_j(p, t_j)) - \tau_i \cdot W_H [I'_i, \pi_i(p, t_i)] \quad (10)$$

Here, $\phi_{i \rightarrow j} = \frac{\alpha_j}{\alpha_i}$ compensates for exposure differences between cameras, τ_k represents inverse exposure time. W_H represents warping of the image patch using homography H across temporal instances.

The complete residual vector, which stacks all intra-camera and Cross-View residuals, is expressed in Eq. (11):

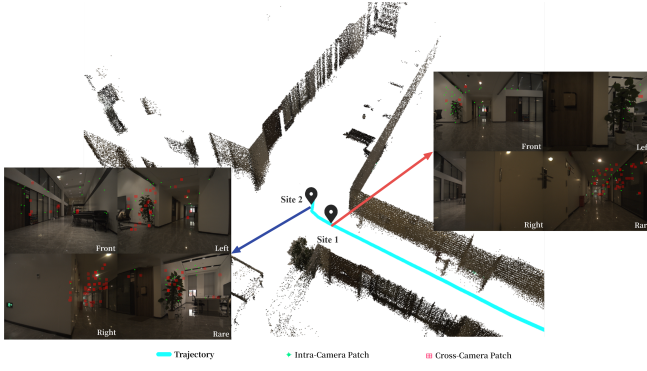


Fig. 4. Illustration of photometric patch migration during turning. The central LiDAR map shows the robot trajectory with two key sites marked. At Site 1, intra-camera patches (green) are consistently tracked within the same camera. At Site 2, the same patches migrate across different cameras, forming Cross-View associations (red). This mechanism preserves photometric continuity across the multi-camera array during turning maneuvers.

$$\mathbf{r}_{\text{total}} = \begin{bmatrix} \mathbf{r}_{\text{direct}}^1 \\ \mathbf{r}_{\text{direct}}^2 \\ \vdots \\ \mathbf{r}_{\text{direct}}^N \\ \mathbf{r}_{\text{migration}}^{1 \rightarrow 2} \\ \mathbf{r}_{\text{migration}}^{1 \rightarrow 3} \\ \vdots \\ \mathbf{r}_{\text{migration}}^{i \rightarrow j} \end{bmatrix} \quad (11)$$

Its dimension accounts for active temporal migrations in the following form:

$$\dim(r_{\text{total}}) = N \cdot P \cdot S + \sum_{M \in \mathcal{A}} P_M \cdot S \quad (12)$$

where $\mathcal{A} = \{(i, j) : \exists p \text{ s.t. } M(p, i \rightarrow j) = 1\}$ represents the set of active migration camera pairs, and P_M denotes the number of migration points for camera pair M .

Finally, migration statistics are accumulated using Eq. (13):

$$\text{Migration count}(p) = \sum_{t=0}^T \sum_{i, j \in \mathcal{C}} M(p, i \rightarrow j, t) \quad (13)$$

where \mathcal{C} represents the camera set, enabling tracking of cumulative Cross-View transitions for each point.

By incorporating temporal migration constraints, the system preserves photometric information beyond single-camera views, extending tracking duration and enhancing geometric diversity. This strengthens pose estimation sensitivity and improves robustness compared to single-camera direct methods, transforming multi-camera tracking from a co-visibility problem into a temporal continuity solution.

C. LiDAR Geometric Constraint Processing

LiDAR measurements provide structural constraints that complement photometric observations in our multi-camera framework. We employ voxel-based plane extraction to efficiently process point clouds and generate geometric residuals.

The raw LiDAR point cloud is discretized into voxels of resolution v_{size} . For each voxel \mathcal{V}_k containing points $\mathcal{P}_k = \{p_i\}_{i=1}^{N_k}$, the sample covariance matrix is computed as:

$$\mathbf{C}_k = \frac{1}{N_k} \sum_{i=1}^{N_k} (p_i - \bar{p}_k)(p_i - \bar{p}_k)^T \quad (14)$$

Planar voxels are identified via eigen-decomposition of \mathbf{C}_k . If the smallest eigenvalue $\lambda_{\min} < \epsilon_{\text{plane}}$, the corresponding eigenvector defines the plane normal \mathbf{n}_k :

$$\mathbf{n}_k^T (p - \bar{p}_k) = 0 \quad (15)$$

Geometric residuals are constructed by projecting transformed LiDAR points p_w onto their corresponding planar surfaces:

$$r_{\text{geo}}(p_w) = \mathbf{n}_k^T p_w + d_k, \quad d_k = -\mathbf{n}_k^T \bar{p}_k \quad (16)$$

These point-to-plane distances serve as direct geometric constraints in the ESIKF framework, providing structural observability that enhances robustness in texture-poor environments.

D. Unified Voxel Mapping with Multi-View Integration

We integrate LiDAR geometry and multi-view photometric patches within a single adaptive volumetric structure. The unified representation employs density-driven octree refinement to balance memory efficiency with spatial accuracy.

1) *Voxel Structure Definition*: Each voxel \mathcal{V}_k encapsulates three components:

$$\mathcal{V}_k = \{\mathcal{G}_k, \mathcal{M}_k, \mathcal{J}_k\} \quad (17)$$

where \mathcal{G}_k represents geometric plane parameters from LiDAR, \mathcal{M}_k contains visual map points with multi-view observations, and \mathcal{J}_k stores octree subdivision structure.

2) *Visual Map Point Generation*: Images are partitioned into regular grids with adaptive sizing. For each grid cell lacking visual map point projections, LiDAR points projecting into that region become candidates for new visual point creation. The system selects the point with highest Shi-Tomasi corner response across all camera views.

3) *Multi-View Observation Management*: Each visual point maintains associated observations as:

$$\mathcal{F}_j = \{\mathcal{P}_j^{(k)}, \mathbf{T}_{wc}^{(k)}, \tau^{(k)}, id_{\text{cam}}^{(k)}\}_{k=1}^{N_{\text{obs}}} \quad (18)$$

where $\mathcal{P}_j^{(k)}$ is the patch organized in multi-level pyramid structure, $\mathbf{T}_{wc}^{(k)}$ is the camera pose, $\tau^{(k)}$ is the exposure parameter, and $id_{\text{cam}}^{(k)}$ is the camera identifier. Updates are triggered when camera pose changes or pixel displacement exceed predefined thresholds. Tukey weighting suppresses photometric outliers during optimization.

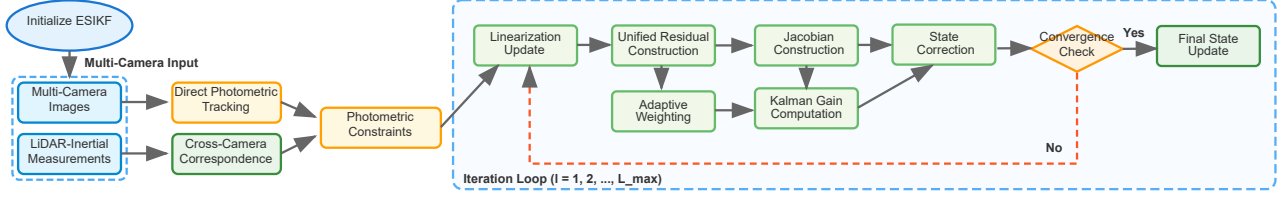


Fig. 5. Iterative Multi-Camera ESIKF Framework. The framework extends standard ESIKF with multi-view integration through: (1) Iterative linearization manages nonlinear photometric residuals from multiple cameras; (2) Joint residual stacking combines LiDAR geometric constraints with multi-camera photometric constraints; (3) Adaptive covariance weighting dynamically adjusts measurement reliability based on each camera’s tracking quality; (4) State increment updates through Kalman filtering until convergence. The multi-modal approach enhances observability and robustness compared to single-sensor estimation.

E. Iterative Multi-Camera State Estimation with ESIKF

We extend the standard ESIKF to integrate multi-view photometric constraints with LiDAR measurements through iterative linearization and adaptive weighting, as shown in Fig. 5.

At each iteration ℓ , the linearization point is updated:

$$\tilde{\mathbf{x}}^{(\ell)} = \hat{\mathbf{x}}_{k|k-1} \boxplus \delta \hat{\mathbf{x}}^{\ell-1} \quad (19)$$

LIO and multi-camera VIO measurements are stacked:

$$\mathbf{r}^{(\ell)} = \begin{bmatrix} \mathbf{r}_{LIO}^{(\ell)} \\ \mathbf{r}_{VIO}^{(\ell)} \end{bmatrix}, \quad \mathbf{H}^{(\ell)} = \begin{bmatrix} \mathbf{H}_{LIO}^{(\ell)} \\ \mathbf{H}_{VIO}^{(\ell)} \end{bmatrix} \quad (20)$$

The Kalman gain and state increment are:

$$\mathbf{K}^{(\ell)} = \mathbf{P}_{k|k-1} (\mathbf{H}^{(\ell)})^T \left[\mathbf{H}^{(\ell)} \mathbf{P}_{k|k-1} (\mathbf{H}^{(\ell)})^T + \mathbf{R}_{\text{multi}} \right]^{-1} \quad (21)$$

$$\delta \hat{\mathbf{x}}^{(\ell)} = \delta \hat{\mathbf{x}}^{(\ell-1)} + \mathbf{K}^{(\ell)} (\mathbf{r}^{(\ell)} - \mathbf{H}^{(\ell)} \delta \hat{\mathbf{x}}^{(\ell-1)}) \quad (22)$$

Eq. (23) defines the adaptive covariance matrix:

$$\mathbf{R}_{\text{multi}} = \text{diag}(\alpha_1 \mathbf{R}_{\text{base}}^{(1)}, \alpha_2 \mathbf{R}_{\text{base}}^{(2)}, \dots, \alpha_{\text{cross}} \mathbf{R}_{\text{cross}}) \quad (23)$$

where scaling factors adapt based on tracking performance:

$$\alpha_i = f \left(\frac{N_{\text{tracked}}^{(i)}}{N_{\text{tracked}}}, \bar{r}_i^2, \text{gradient}_i \right) \quad (24)$$

The complete algorithm implementation is summarized below:

IV. EXPERIMENTAL EVALUATION

To demonstrate the robustness and accuracy of the proposed method, we evaluated it on the Hilti SLAM Challenge 2022 [24] and Newer College datasets [25]. In particular, we evaluated the absolute trajectory error (RMSE) between the ground truth pose provided in the datasets and the trajectory estimated by the proposed method; we compared this with the results of other state-of-the-art methods, such as FAST-LIVO2 [12], FAST-LIVO [9], R3LIVE [17], FAST-LIO2 [15], and OpenMAVIS [11]. We also collected LiDAR scan data using LIVOX MID360 and four synchronized cameras in custom multi-camera configurations.

Algorithm 1 ESIKF

- 1: Synchronize multi-camera images, LiDAR, and IMU
- 2: IMU forward propagation: $\hat{\mathbf{x}}^-, \mathbf{P}^-$
- 3: LiDAR point motion compensation and plane extraction
- 4: **LiDAR update:** Point-to-plane residuals \mathbf{r}_{LIO}
- 5: Select photometric patches from each camera $c \in [1, C]$
- 6: $\ell \leftarrow 0, \delta \hat{\mathbf{x}}^{(0)} \leftarrow \mathbf{0}$
- 7: **repeat**
- 8: $\ell \leftarrow \ell + 1$; Update $\tilde{\mathbf{x}}^{(\ell)} = \hat{\mathbf{x}}^- \boxplus \delta \hat{\mathbf{x}}^{(\ell-1)}$
- 9: **for** camera $c = 1, \dots, C$ **do**
- 10: Compute $\mathbf{r}_c^{(\ell)} = \mathbf{I}_{ref} - \mathbf{I}_c(\pi_c(\mathbf{X}^w))$, $\mathbf{H}_c^{(\ell)}$
- 11: **end for**
- 12: Stack: $\mathbf{r}^{(\ell)} = [\mathbf{r}_{LIO}; \mathbf{r}_{VIO}]$, $\mathbf{H}^{(\ell)} = [\mathbf{H}_{LIO}; \mathbf{H}_{VIO}]$
- 13: Adaptive covariance: $\mathbf{R}_{\text{multi}} = \text{diag}(\alpha_1 \mathbf{R}_1, \dots, \alpha_C \mathbf{R}_C)$
- 14: Kalman update: $\delta \hat{\mathbf{x}}^{(\ell)} = \delta \hat{\mathbf{x}}^{(\ell-1)} + \mathbf{K}^{(\ell)} (\mathbf{r}^{(\ell)} - \mathbf{H}^{(\ell)} \delta \hat{\mathbf{x}}^{(\ell-1)})$
- 15: **until** convergence
- 16: Final update: $\hat{\mathbf{x}}_{k|k} = \hat{\mathbf{x}}^- \boxplus \delta \hat{\mathbf{x}}^{(\ell)}$
- 17: **return** $\hat{\mathbf{x}}_{k|k}, \mathbf{P}_{k|k}$

A. Datasets and Baselines

Public Benchmarks: Hilti SLAM Challenge 2022 [24] provides construction site sequences with millimeter-accurate ground truth via laser metrology. Newer College Dataset [25] includes campus and underground environments with challenging lighting and viewpoint changes.

Custom Dataset: We collected data using a LIVOX MID360 LiDAR (360 $\hat{\text{A}}^\circ$ FoV, 10Hz) and four cameras (1024 \times 768, 10Hz) in a cross-pattern configuration. The acquisition platforms include both a handheld device and a robot-mounted device, as illustrated in Fig. 6.

Baselines: FAST-LIVO2, FAST-LIVO, R3LIVE (LiDAR-inertial-visual), FAST-LIO2 (LiDAR-inertial), and OpenMAVIS (multi-camera visual-inertial, evaluated where compatible).

TABLE I
ABSOLUTE TRAJECTORY ERRORS (RMSE, METERS)

Dataset	Sequence	FAST-LIVO	FAST-LIVO2	R3LIVE	FAST-LIO2	OpenMAVIS	Omni-LIVO
Hilti SLAM Challenge	Exp04 Construction Upper Level 1	1.9525	0.0356	0.0276	0.124	0.0825	0.0266
	Exp05 Construction Upper Level 2	0.1654	0.0414	0.0254	0.0996	0.0398	0.024
	Exp06 Construction Upper Level 3	×	0.1883	0.0486	×	0.0752	0.0434
	Exp10 Cupola 2	×	0.2323	×	×	0.1363	0.117
	Exp14 Basement 2	×	0.0484	0.0971	0.1361	0.0816	0.0429
	Exp16 Attic to Upper Gallery 2	×	0.3284	×	×	0.2546	0.1197
	Exp18 Corridor Lower Gallery 2	×	0.2007	×	×	0.1782	0.1144
Newer College (Campus)	quad-easy	20.2697	0.0818	0.0862	0.0923	0.0836	0.0706
	quad-medium	22.403	0.0733	0.0606	0.1007	0.1127	0.0648
	quad-hard	22.8138	0.0825	0.0705	0.1462	0.1239	0.0569
	stairs	×	0.0556	0.2236	×	×	0.0492
Newer College (Underground)	underground-easy	0.7755	0.0487	0.0371	0.1564	0.1202	0.0489
	underground-medium	8.6613	0.0434	0.047	0.1533	0.1298	0.0336
	underground-hard	11.0177	0.2414	0.0686	0.1414	0.2553	0.0547



(a) Handheld device setup



(b) Robotic platform setup

Fig. 6. SLAM data acquisition platforms used in our custom dataset. (a) Handheld configuration. (b) Robotic configuration.

B. Quantitative Results

Table I summarizes absolute trajectory errors (RMSE) across all sequences. Omni-LIVO achieves the lowest error in 11 out of 14 sequences and successfully completes all evaluated tracks, demonstrating superior accuracy and robustness.

On challenging Hilti sequences, FAST-LIVO fails in 5/7 cases and FAST-LIO2 in 4/7, while Omni-LIVO completes all with sub-centimeter to decimeter accuracy. In Newer College underground scenarios with severe illumination changes, Omni-LIVO maintains consistent performance (0.0336–0.0547 m) while FAST-LIVO exhibits catastrophic drift (8–11 m).

Omni-LIVO demonstrates superior consistency with lowest standard deviations across all environment types, indicating robust performance regardless of scene complexity. The method maintains sub-decimeter accuracy even in the most challenging scenarios where competing approaches exhibit meter-level drift.

C. Computational Performance

Table II reports processing times on the Exp04 Construction Upper Level 1 sequence from the Hilti SLAM Challenge, representing a typical indoor construction environment with moderate computational demands. All experiments were conducted on a laptop with an Intel Core i9-13900HX processor, NVIDIA GeForce RTX 4070 Laptop GPU, and 32GB RAM. Since a direct comparison with pure visual methods is not

meaningful, we evaluate against LiDAR+inertial+visual odometry (LIVO) systems. In our evaluation, Omni-LIVO processes three synchronized cameras (front, left, right) in real time, with only a moderate overhead (1.19 \times) compared to the single-camera FAST-LIVO2 baseline.

D. Trajectory and Mapping Analysis

Visual trajectory comparisons in Fig. 7 demonstrate Omni-LIVO’s robustness across challenging sequences. In Exp06, rapid rotations cause single-camera tracking failures, while Omni-LIVO maintains consistency through Cross-View temporal migration. Exp16 involves multi-level transitions where the multi-camera array provides spatial redundancy. In Underground-hard with extreme illumination variations, competing methods exhibit meter-level drift while Omni-LIVO maintains sub-decimeter accuracy through adaptive covariance weighting.

The mapping quality comparison in Fig. 8 highlights multi-camera integration advantages for scene reconstruction. Traditional single-camera systems produce sparse colorization with coverage gaps, while Omni-LIVO’s multi-camera configuration provides dense, uniform colorization through comprehensive spatial observation.

Table III quantifies the RGB point cloud generation capabilities across different sequences. Omni-LIVO consistently produces 2-4 \times more RGB-colored points than competing methods, with particularly significant improvements in complex environments like basement3 (3.5 \times more than FAST-LIVO2). The multi-camera configuration enables comprehensive colorization even in challenging scenarios where single-camera approaches exhibit severe coverage limitations.

E. Discussion

Omni-LIVO achieves the lowest RMSE on 12 out of 14 sequences with an average 34% accuracy improvement over FAST-LIVO2. The system successfully completes all 14 sequences from challenging datasets while competing methods fail on 5-7 sequences. The multi-camera configuration generates significantly denser RGB-colored point cloud data

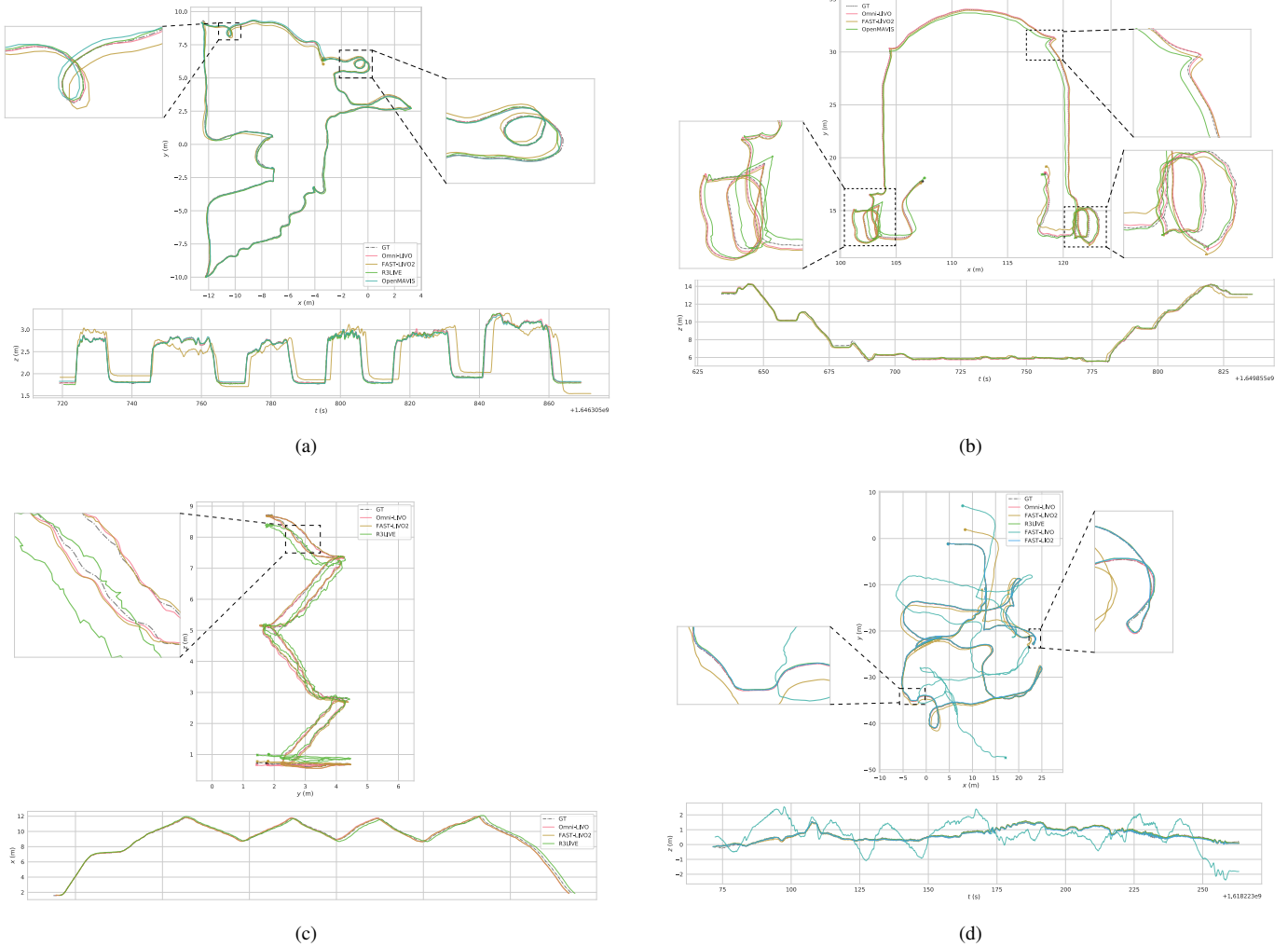


Fig. 7. Trajectory comparison on challenging sequences: (a) Exp06 with rapid rotations causing single-camera tracking failures, where Omni-LIVO maintains consistency through Cross-View temporal migration; (b) Exp16 with multi-level transitions and vertical movements, showing multi-camera array preserves continuity during aggressive 3D maneuvers; (c) Stairs with complex helical motion, where LiDAR-visual fusion provides enhanced observability; (d) Underground-hard with extreme illumination variations, demonstrating robust performance through adaptive covariance weighting while other methods exhibit drift or failure.

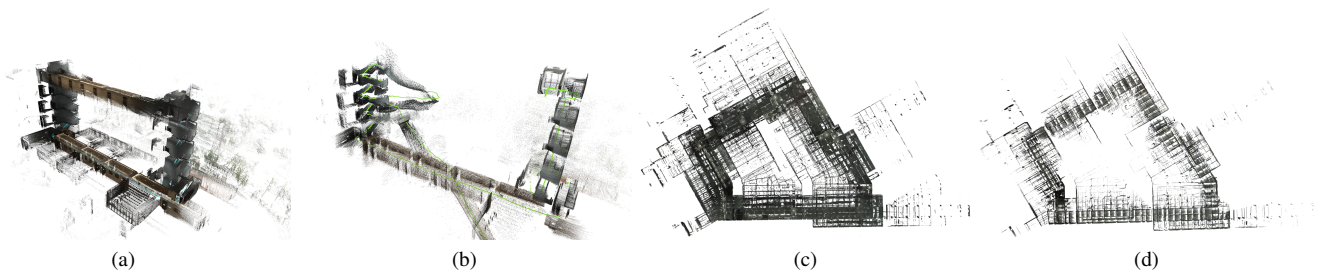


Fig. 8. Mapping quality comparison: (a) Omni-LIVO multi-floor reconstruction with dense colorization from four-camera coverage; (b) R3LIVE single-camera result showing sparse colorization and incomplete coverage; (c) Omni-LIVO underground mapping with dense multi-camera colorization despite lighting variations; (d) FAST-LIVO underground result with degraded reconstruction quality and significant gaps.

(Table III), with up to $3.5\times$ improvement over single-camera approaches.

These results demonstrate that Cross-View temporal migration effectively bridges the field-of-view mismatch between wide-angle LiDAR sensors and narrow-FoV cameras. The uni-

fied voxel mapping framework provides comprehensive scene colorization with minimal coverage gaps while maintaining only moderate computational overhead ($1.19\times$ compared to FAST-LIVO2).

TABLE II
COMPUTATIONAL PERFORMANCE COMPARISON ON EXP04
CONSTRUCTION UPPER LEVEL 1

Method	Avg. Time (ms)	Memory (MB)	Max Freq. (Hz)
FAST-LIVO	25.2	3884	39.7
FAST-LIVO2	30.7	4225	32.6
R3LIVE	28.5	5423	35.1
Omni-LIVO	35.5	5961	28.2

TABLE III
RGB POINT CLOUD STATISTICS (NUMBER OF COLORED POINTS)

Method	stairs	classroom	basement3	corridor
Omni-LIVO	6,436,111	4,484,889	33,513,608	8,715,790
FAST-LIVO2	6,767,543	3,111,504	9,519,125	4,863,001
FAST-LIVO	3,827,955	1,611,539	5,019,200	2,543,585
R3LIVE	393,242	619,310	1,213,929	1,007,194

V. CONCLUSION

This letter presents Omni-LIVO, a tightly coupled multi-camera LiDAR-inertial-visual odometry system that bridges the field-of-view mismatch between wide-angle LiDAR and conventional cameras through Cross-View patch migration and adaptive multi-view ESIKF integration. Experimental validation demonstrates 23% RMSE reduction and 100% completion rate across challenging sequences. The multi-camera configuration maintains photometric patch continuity across non-overlapping views, improving system robustness. Future work will address online loop closure and multi-sensor calibration.

REFERENCES

- J. Engel, T. Schödl, and D. Cremers, "LSD-SLAM: Large-scale direct monocular SLAM," in *Proc. Eur. Conf. Comput. Vis. (ECCV)*, Zurich, Switzerland, Sep. 2014, pp. 834–849, doi: 10.1007/978-3-319-10605-2_54.
- R. Mur-Artal and J. D. Tardós, "ORB-SLAM2: An open-source SLAM system for monocular, stereo, and RGB-D cameras," *IEEE Trans. Robot.*, vol. 33, no. 5, pp. 1255–1262, Oct. 2017, doi: 10.1109/TRO.2017.2705103.
- J. Zhang and S. Singh, "LOAM: Lidar odometry and mapping in real-time," in *Proc. Robot.: Sci. Syst.*, Berkeley, CA, USA, Jul. 2014, doi: 10.15607/RSS.2014.X.007.
- J. Tang, Y. Chen, X. Niu, L. Wang, L. Chen, J. Liu, C. Shi, and N. El-Sheimy, "LiDAR scan matching aided inertial navigation system in GNSS-denied environments," *Sensors*, vol. 15, no. 7, pp. 16710–16728, Jul. 2015, doi: 10.3390/s150716710.
- S. Chen, B. Zhou, C. Jiang, W. Xue, and Q. Li, "A LiDAR/visual SLAM backend with loop closure detection and graph optimization," *Sensors*, vol. 18, no. 12, art. no. 4377, Dec. 2018, doi: 10.3390/s18124377.
- T. Qin, P. Li, and S. Shen, "VINS-Mono: A robust and versatile monocular visual-inertial state estimator," *IEEE Trans. Robot.*, vol. 34, no. 4, pp. 1004–1020, Aug. 2018, doi: 10.1109/TRO.2018.2853729.
- C. Campos, R. Elvira, J. J. G. Rodríguez, J. M. M. Montiel, and J. D. Tardós, "ORB-SLAM3: An accurate open-source library for visual, visual-inertial, and multimap SLAM," *IEEE Trans. Robot.*, vol. 37, no. 6, pp. 1874–1890, Dec. 2021, doi: 10.1109/TRO.2021.3075644.
- T. Shan, B. Englot, D. Meyers, W. Wang, C. Ratti, and D. Rus, "LIO-SAM: Tightly-coupled lidar inertial odometry via smoothing and mapping," in *Proc. IEEE/RSJ Int. Conf. Intell. Robot. Syst. (IROS)*, Las Vegas, NV, USA, Oct. 2020, pp. 5135–5142, doi: 10.1109/IROS45743.2020.9341176.
- C. Zheng, Q. Zhu, W. Xu, X. Liu, Q. Guo, and F. Zhang, "FAST-LIVO: Fast and tightly-coupled sparse-direct LiDAR-inertial-visual odometry," in *Proc. IEEE/RSJ Int. Conf. Intell. Robot. Syst. (IROS)*, Kyoto, Japan, Oct. 2022, pp. 4003–4009, doi: 10.1109/IROS47612.2022.9981107.
- W. Kuo, Y. Lin, P. Liao, H. Chen, and C. Chien, "Redesigning SLAM for arbitrary multi-camera systems," in *Proc. IEEE Int. Conf. Robot. Autom. (ICRA)*, Paris, France, May 2020, pp. 4675–4681, doi: 10.1109/ICRA40945.2020.9196730.
- Y. Wang, Y. Ng, I. Sa, A. Parra, C. Rodriguez-Opazo, T. Lin, and H. Li, "MAVIS: Multi-camera augmented visual-inertial SLAM using SE₂(3)-based exact IMU pre-integration," in *Proc. IEEE Int. Conf. Robot. Autom. (ICRA)*, Yokohama, Japan, May 2024, pp. 1694–1700, doi: 10.1109/ICRA57147.2024.10609982.
- C. Zheng, W. Xu, Q. Guo, and F. Zhang, "FAST-LIVO2: Fast, direct LiDAR-inertial-visual odometry," *IEEE Trans. Robot.*, vol. 40, pp. 1529–1546, 2024, doi: 10.1109/TRO.2024.3502198.
- T. Shan and B. Englot, "LeGO-LOAM: Lightweight and ground-optimized lidar odometry and mapping on variable terrain," in *Proc. IEEE/RSJ Int. Conf. Intell. Robot. Syst. (IROS)*, Madrid, Spain, Oct. 2018, pp. 4758–4765, doi: 10.1109/IROS.2018.8594299.
- W. Xu, Y. Cai, D. He, J. Lin, and F. Zhang, "FAST-LIO2: Fast direct LiDAR-inertial odometry," *IEEE Trans. Robot.*, vol. 38, no. 4, pp. 2053–2073, Aug. 2022, doi: 10.1109/TRO.2022.3141876.
- W. Xu and F. Zhang, "FAST-LIO: A fast, robust LiDAR-inertial odometry package by tightly-coupled iterated Kalman filter," *IEEE Robot. Autom. Lett.*, vol. 6, no. 2, pp. 3317–3324, Apr. 2021, doi: 10.1109/LRA.2021.3064227.
- J. Lin and F. Zhang, "R²LIVE: A robust, real-time, LiDAR-inertial-visual tightly-coupled state estimator and mapping," *IEEE Robot. Autom. Lett.*, vol. 6, no. 4, pp. 7469–7476, Oct. 2021, doi: 10.1109/LRA.2021.3095515.
- J. Lin and F. Zhang, "R³LIVE: A robust, real-time, RGB-colored, LiDAR-inertial-visual tightly-coupled state estimation and mapping package," in *Proc. IEEE Int. Conf. Robot. Autom. (ICRA)*, Philadelphia, PA, USA, May 2022, pp. 10672–10678, doi: 10.1109/ICRA46639.2022.9812253.
- K. Eickenhoff, P. Geneva, and G. Huang, "MIMC-VINS: A versatile and resilient multi-IMU multi-camera visual-inertial navigation system," *IEEE Trans. Robot.*, vol. 37, no. 5, pp. 1360–1374, Oct. 2021, doi: 10.1109/TRO.2021.3062254.
- Z. Zhang, S. Karaman, and N. Roy, "BAMF-SLAM: Bundle adjusted multi-fisheye visual-inertial SLAM using recurrent field transforms," in *Proc. IEEE Int. Conf. Robot. Autom. (ICRA)*, London, UK, May 2023, pp. 5401–5407, doi: 10.1109/ICRA48891.2023.10161181.
- R. A. Newcombe, S. J. Lovegrove, and A. J. Davison, "DTAM: Dense tracking and mapping in real-time," in *Proc. IEEE Int. Conf. Comput. Vis. (ICCV)*, Barcelona, Spain, Nov. 2011, pp. 2320–2327, doi: 10.1109/ICCV.2011.6126513.
- J. Engel, V. Koltun, and D. Cremers, "Direct sparse odometry," *IEEE Trans. Pattern Anal. Mach. Intell.*, vol. 40, no. 3, pp. 611–625, Mar. 2018, doi: 10.1109/TPAMI.2017.2658577.
- R. Wang, M. Schworer, and D. Cremers, "Stereo DSO: Large-scale direct sparse visual odometry with stereo cameras," in *Proc. IEEE Int. Conf. Comput. Vis. (ICCV)*, Venice, Italy, Oct. 2017, pp. 3903–3911, doi: 10.1109/ICCV.2017.421.
- S. Urban and S. Hinz, "MultiCol-SLAM: A modular real-time multi-camera SLAM system," arXiv preprint, Oct. 2016. [Online]. Available: <https://arxiv.org/abs/1610.07336>
- L. Zhang, M. Helmberger, L. F. T. Fu, D. Wisth, M. Camurri, D. Scaramuzza, and M. Fallon, "Hilti Oxford dataset: A millimetre accurate benchmark for simultaneous localization and mapping," *IEEE Robot. Autom. Lett.*, vol. 8, no. 1, pp. 408–415, Jan. 2023, doi: 10.1109/LRA.2022.3226077.
- L. Zhang, M. Camurri, D. Wisth, and M. Fallon, "Multi camera LiDAR inertial extension to the newer college dataset," arXiv preprint, Dec. 2021. [Online]. Available: <https://arxiv.org/abs/2112.08854>